Ground Penetrating Radar
The first peer-reviewed scientific journal dedicated to GPR

MODEL-BASED CLUTTER REDUCTION METHOD FOR FORWARD LOOKING GROUND PENETRATING RADAR IMAGING

YUKINORI FUSE[1], BORJA GONZALEZ-VALDES[2],
JOSE A. MARTINEZ-LORENZO[1] & CAREY M. RAPPAPORT[1]

[1] DEPARTMENT OF ELECTRICAL AND COMPUTER ENGINEERING, NORTHEASTERN UNIVERSITY, BOSTON, MASSACHUSETTS, UNITED STATES OF AMERICA – YFUSE@ECE.NEU.EDU; JMARTINE@ECE.NEU.EDU; RAPPAPORT@COE.NEU.EDU

[2] UNIVERSITY OF VIGO, VIGO, SPAIN – BGVALDES@COM.UVIGO.ES

ABSTRACT

Model based imaging methods for a dual-band fully polarimetric vehicle-based Forward-Looking Ground Penetrating Radar (FLGPR) are presented. The radar consists of two fully polarimetric arrays of wideband horns - one at L-band and one at X-band - that form synthetic apertures as the vehicle advances. Model-based clutter suppression image processing is used to clean the Synthetic Aperture Radar (SAR) image obtained from the VV polarized L-band radar by employing a mixed binary mask. This clutter mask is formed from the second (X-band) frequency and the VH cross-polarized L-band responses. Receiver Operating Characteristic (ROC) curves using measured field data are used to evaluate the enhancement of the target signal to clutter ratio. The proposed methods reduce the false alarm rate and improve the detection performance of the system.

KEYWORDS: Imaging system; Synthetic Aperture Radar (SAR); Forward-Looking Ground Penetrating Radar (FLGPR).

1. INTRODUCTION

Ground Penetrating Radar (GPR) is widely used to detect subsurface objects [1] including explosive devices such as mines and Improvised Explosive Devices (IEDs). Other detection sensors include infrared (IR) cameras [2], [3], acoustic detectors [4], and laser-induced breakdown spectroscopy [5]. Forward-Looking Ground Penetrating Radar (FLGPR) has the advantages of sensing below the ground surface while having a large stand-off distance between the sensor systems and buried threats, and covering a wide detection area [6], [7]. These advantages lead to improved safety and efficiency for operators during the detection process. However, a major problem with FLGPR is clutter resulting from

https://doi.org/10.26376/GPR2018011

scattering from the rough ground surface; including large rocks, large depressions, and objects on the surface like trees, bushes, and manmade items. It is important to suppress this clutter from on- or above-ground objects in order to detect threatening objects below the ground surface and reduce the false alarm rate. Several methods have been proposed to solve this problem. One approach is based on extracting the characteristics and features of the target signal and classifying the received signals to extract the target signals from FLGPR image [8]–[10]. Another reduces the false alarms by combining FLGPR image results with other types the sensors. Combined FLGPR and IR sensor information has been studied in [11], [12]. The IR features are extracted from a vehicle mounted IR camera and IR images provide the clutter locations, which are not available in FLGPR, to eliminate false alarms. Another sensor combination (FLGPR and visible-spectrum colour camera) has been studied in [13]. The information from the visible camera is used for reducing the false alarms. FLGPR image data is used directly while the camera is used to extract the features of the target signals or eliminate the clutter. In this work, a model-based clutter suppression method is presented. The method is validated with field measurement data experimentally generated by the United States (US) Army, Communications-Electronics Research, Development and Engineering Center (CERDEC), Night Vision and Electronic Sensors Directorate (NVESD). The FLGPR system is a dual-band radar system with L-band (0.75 ~ 3.2 GHz) and X-band (8 ~ 12 GHz) radars (Table I).

The L-band radar is fully polarimetric while X-band radar is VV (vertical transmitting, vertical receiving) - polarized. The scattering from above-ground objects tends to be strong for both X-band and L-band radar, while the X-band and the VH (vertical transmitting, horizontal receiving) cross-polarization responses of buried targets are weak. This is due to higher frequency waves being attenuated as they propagate through soil, and the depolarizing effects of the wave refraction at the ground interface for VH scattered waves. Using X-band and VH L-band signals to identify clutter signals with minimal response from subsurface objects provides a method to uniquely distinguish buried targets. The model-based response at the receiving array due to the primary clutter objects is subtracted from the original VV polarized L-band signal, and a new clutter-suppressed Synthetic Aperture Radar (SAR) image is generated.

https://doi.org/10.26376/GPR2018011

TABLE I – FLGPR SYSTEM.

	L-band radar	**X-band radar**
Antennas	8 transmitters, 8 receivers	32 transmitters, 4 receivers
Frequency bandwidth	0.75 GHz – 3.2 GHz	8.4 GHz – 10.4 GHz
Polarization	VV, HH, VH, HV	VV

2. MODEL BASED CLUTTER SUPPRESSION METHOD

This section presents the methodology for selectively suppressing above-ground clutter. The proposed dual-wideband FLGPR system properties are described in Table I. The L-band radar has 8 transmitters and 8 receivers, and the X-band radar has 32 transmitters and 4 receivers. A Global Positioning System (GPS) is mounted on the system so that the array position can be obtained at each location. The reconstructed wideband array based images can be added together coherently with using multiple frames in range direction to form SAR image.

The main steps of this method are as follows:

Step 1) Generate the VV L-band SAR image.
Step 2) Generate the VH L-band SAR image.
Step 3) Generate the VV X-band SAR image.
Step 4) Segment the reconstruction area into four sub-regions in range for separate processing.
Step 5) Form binary masks with a 1 at pixels with reflectivity above - or 0 for reflectivity below - a given threshold.
Step 6) Multiply the original image from 1) with the binary masks.
Step 7) Model the response at the L-band receiving antenna array due to just the masked reconstructions at each sub-region.
Step 8) Compute the VV L-band SAR image from the cleaned response.

2.1 SAR imaging and reflectivity reconstruction

The reflectivity of all objects in the imaging area is reconstructed using wideband array-based radar imaging as given by:

https://doi.org/10.26376/GPR2018011

$$x(X_p, Y_p) = \sum_n^N \sum_m^M \sum_k^K b(f_k)\ exp\left[j\frac{2\pi f_k}{c} L_{mn}(X_p, Y_p)\right] \quad (1)$$

where x is output SAR image pixel value, $b(f_k)$ is measured observed data set, f_k is the k^{th} operating frequency and $L_{mn}(X_p, Y_p)$ is the total path length between the n^{th} transmitter at $(X_{trs,n}, Y_{trs,n}, Z_{trs,n})$ to the p^{th} image pixel at (X_p, Y_p), and then to the m^{th} receiver at $(X_{rcv,m}, Y_{rcv,m}, Z_{rcv,m})$. So $L_{mn}(X_p, Y_p)$ can be expressed as:

$$L_{mn}(X_p, Y_p) = \sqrt{(X_{rcv,m} - X_p)^2 + (Y_{rcv,m} - Y_p)^2 + Z_{rcv,m}^2} + \sqrt{(X_{trs,n} - X_p)^2 + (Y_{trs,n} - Y_p)^2 + Z_{trs,n}^2} \quad (2)$$

The geometry of the FLGPR imaging system is shown in Figure 1.

Equation (1) can be expressed in a reshaped matrix form approximate solution given by [14]:

$$\mathbf{x} = \mathbf{A}^{\dagger} \cdot \mathbf{b} \quad (3)$$

where $\mathbf{x}$ and $\mathbf{b}$ are $p \times 1$ and $mnk \times 1$ column matrices representing the reflectivities (or image) and the measured radar responses, respectively, and $\mathbf{A}^{\dagger}$ is the adjoint (conjugate transpose) of the scattering matrix $\mathbf{A}$. The image x can be added coherently for multiple frames in the down-track direction. The final SAR image is given by the coherent (complex) sum:

$$x_{multi}(X_p, Y_p) = \sum_{fr} x(X_p, Y_p) \quad (4)$$

where fr is the number of frames in the range direction.

2.2 Mask formulation

A binary mask is derived from the L-band VV polarization, VH polarization, and the X-band VV polarization SAR images. The imaging area is nominally divided into four sub-regions. This is necessary to compensate for the spreading of the radiated waves, which reduces the amplitude of the received signals from distant scatterers. The binary mask $\mathbf{m}$ is generated by finding the pixel values with magnitude exceeding a given threshold and setting them to 1, while all other pixels are set to 0. The details of the procedure of the mask formulation are in Sub-section 2.4.

https://doi.org/10.26376/GPR2018011

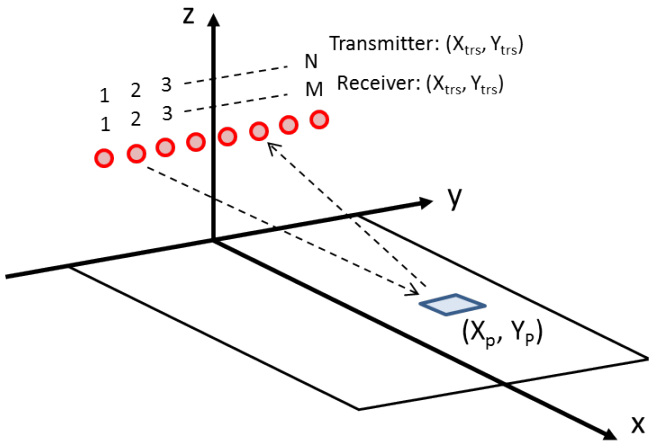

FIG. 1 – Imaging system geometry.

2.3 Masking L-band data

A matrix is overlaid on the original L-band image by simply multiplying pixel by pixel: $\hat{x}_i = m_i x_i$. The $\hat{\mathbf{x}}$ image is now used to derive the new simulated observed clutter-only response $\hat{\mathbf{b}}$ given by:

$$\widehat{\mathbf{b}} = \mathbf{A} \cdot \hat{\mathbf{x}} \tag{5}$$

Finally, the new suppressed clutter image $\mathbf{x}'$ is expressed as:

$$\mathbf{x}' = \mathbf{A}^{\dagger} \cdot (\mathbf{b} - B\hat{\mathbf{b}}) \tag{6}$$

where B is a normalizing amplitude adjustment coefficient. B is expressed as the ratio between the maximum magnitudes of $\hat{\mathbf{x}}$ and the maximum magnitudes of the SAR image $\mathbf{x}'_2$ given by the new cleaned measured response $\hat{\mathbf{b}}$. The amplitude adjustment coefficient B can be written as:

$$B = Max(\hat{\mathbf{x}})/Max\,(\mathbf{x}'_2) \tag{7}$$

with

$$\mathbf{x}'_2 = \mathbf{A}^{\dagger} \cdot \hat{\mathbf{b}} \tag{8}$$

In the case of the plural masks in one image, B has to be derived in each sub-region area, respectively, to obtain the best-subtracted SAR image. In addition, this procedure can be used repeatedly to suppress the clutter signals using the same mask in each frame. The effect of this iteration is shown in the following sections.

https://doi.org/10.26376/GPR2018011

2.4 Mask creation procedure

The procedure for combining the L-band VV, VH, and X-band masks is presented in this subsection. The masking image is derived from L-band VV pol, VH pol SAR images and the X-band SAR image. The pixel values with magnitude exceeding a given threshold are set to 1, while all other pixels are set to 0, creating a binary mask row matrix.

The masking area is created based on the shape of the L-band VV pol mask, because these regions constitute the dominant clutter in the simulated SAR image. The region shapes are weighted with the other sensor data to ensure that they do not represent target signal responses. The combination of the responses are eventually subtracted from the original L-band VV polarization received signals. The concept of mask creation is described in Figure 2. The final mask is composed of two parts: the fundamental part and the extended part. Fundamental part is able to cover the most part of the clutter region, however when some large clutter signals exist at the roadside, they could be potential false alarms. The spatially filtered mask with a lower threshold can be applied only for the roadside region. In the fundamental part of the mask, each region of L-band VH pol binary mask and X-band binary mask is compared to the region of L-band VV pol binary mask, and the intersection is selected as the masking area. The combined L-band VV and VH pol mask and the combined L-band VV and X-band binary mask are added to form the final mixed binary mask. The thresholds are selected from calibration cases to be as low as possible without compromising the target signal response.

In the extended part, the masks are formed with the lower threshold to cover a wider clutter area. The region of L-band VH pol binary mask with a lower threshold is compared to the region of L-band VV pol binary mask with a similar lower threshold. In addition, the L-band VH pol binary mask with a lower threshold is used as one of the selected masking areas. The union of the binary masks forms the final masking image for the extended part. Afterward, the combined mask is spatially selected for the roadside area: -10 ~ -4 m and 4 ~ 10 m in cross-range, and added to the final mask for the fundamental part. The thresholds are derived by the average valued of the road-side clutter in a frame in test lane.

https://doi.org/10.26376/GPR2018011

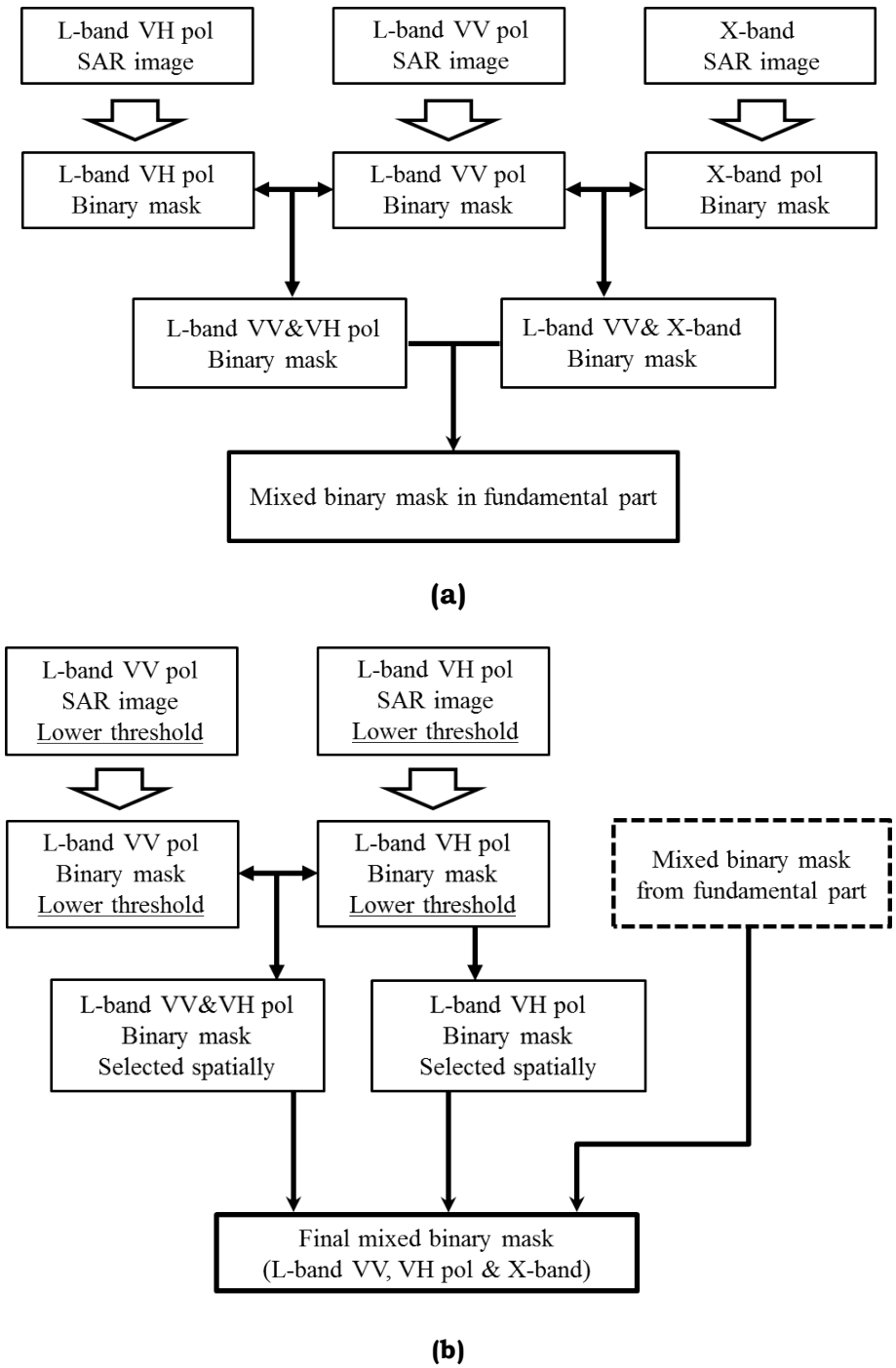

FIG. 2 – Procedure of the mask creation: **(a)** Fundamental part of the mask; **(b)** Extended part of the mask.

https://doi.org/10.26376/GPR2018011

3. RESULTS

3.1 Mask effectiveness

Examples of the fundamental part of each SAR image, and binary mask of L-band VV pol, VH-pol, and X-band radar are presented from Figure 3 [15] to Figure 5. Figure 6 shows the mixed binary mask for the fundamental part and the extended part. Green triangle marker shows the buried target position. In this case, some targets are buried at almost the same location. It is observed that the mixed binary mask covers just the clutter area and not the target image positions.

3.2 Iterative clutter suppression method

The effect of iteration on the masking process with multiple frames is presented. The $\hat{\mathbf{b}}$ in (5) is obtained with the L-band VV polarization image multiplied by the mixed binary mask, and the new processed SAR image is created. This procedure can be applied repeatedly until the clutter signal is sufficiently suppressed. The process is applied iteratively up to 7 times, with the goal of reducing the clutter power below the power of the buried target images.

The processed images can be combined by coherent averaging. Several combinations are proposed in Table II and some examples of masking process results are presented in Figure 7. The representative clutter power levels are chosen from two clutter regions which are highlighted with light green rectangles in Figure 3(a). Based on this figure, by increasing the number of iterations, the clutter power is getting smaller while the target signals still remain. The effect of these combinations is quantified in Figure 8(a), and Figure 8(b) shows the result without coherent averaging, for comparison.

The clutter signals are mixed and effectively cancelled out by taking the average of multiple iterations. The clutter signal's power is decreased about 26.5 dB compared to the original SAR image. It indicates achieving about 5.03 dB reductions in the clutter signal's power by combining the images. The combination of smaller intensities (6 and 7 times iterations) produces the best pattern in this consideration.

https://doi.org/10.26376/GPR2018011

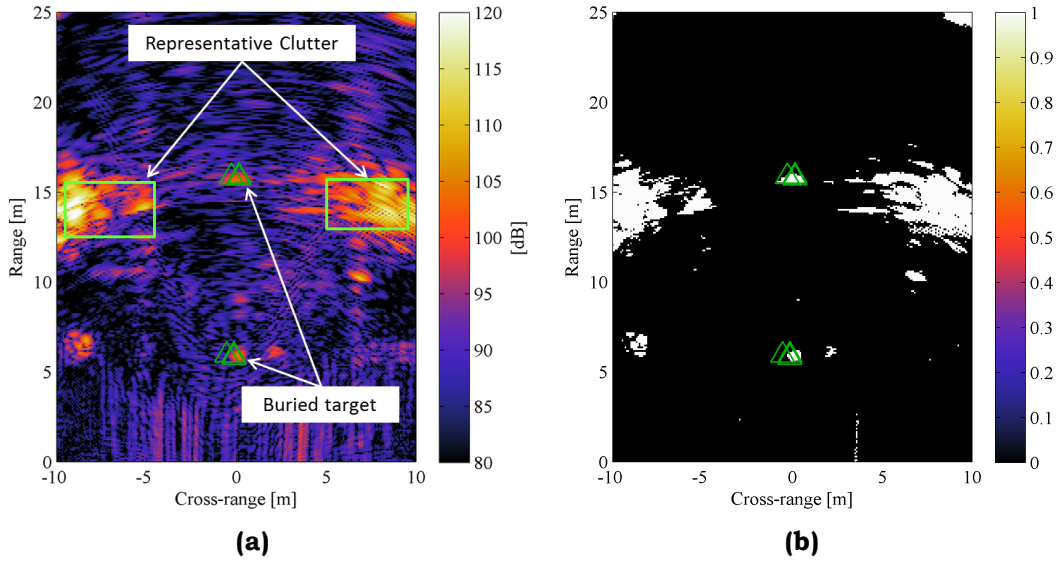

FIG. 3 – L-band VV pol result: **(a)** SAR image [15]; **(b)** Binary mask image for fundamental part. (Δ : True buried target position)

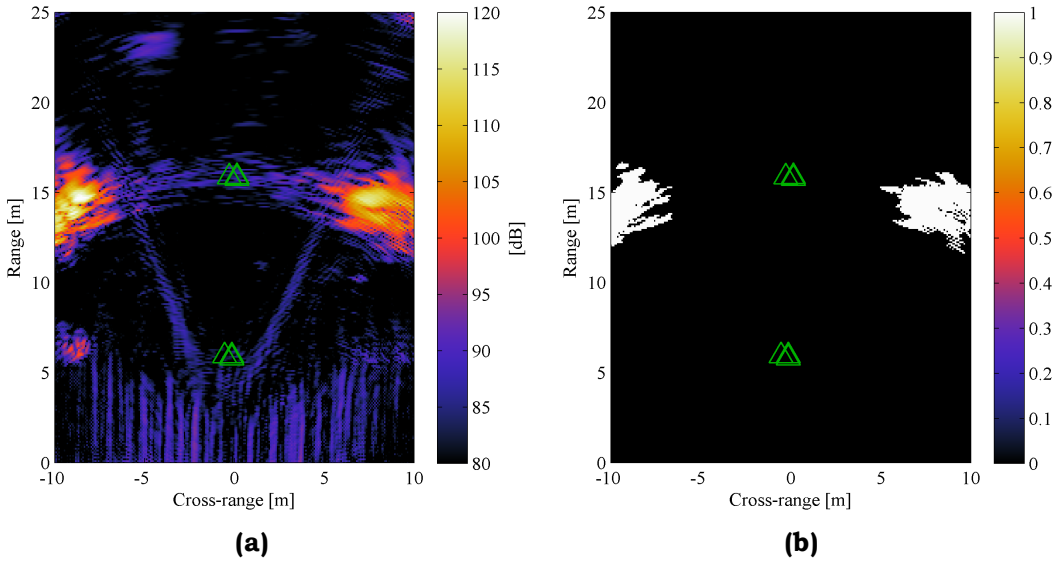

FIG. 4 – L-band VH pol result: **(a)** SAR image; **(b)** Binary mask image for fundamental part. (Δ : True buried target position)

https://doi.org/10.26376/GPR2018011

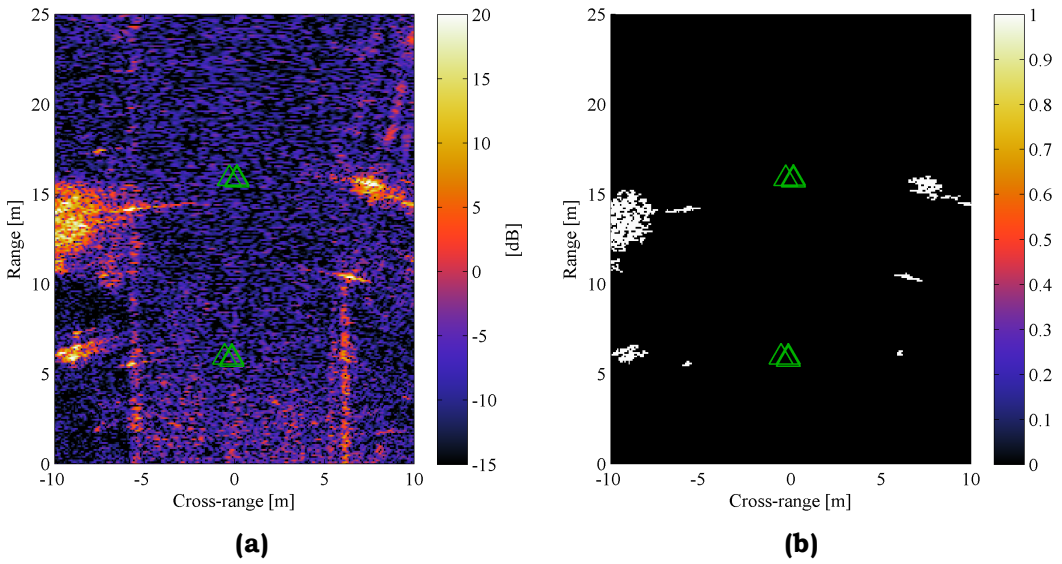

FIG. 5 – X-band result: **(a)** SAR image; **(b)** Binary mask image for fundamental part (Δ : True buried target position.)

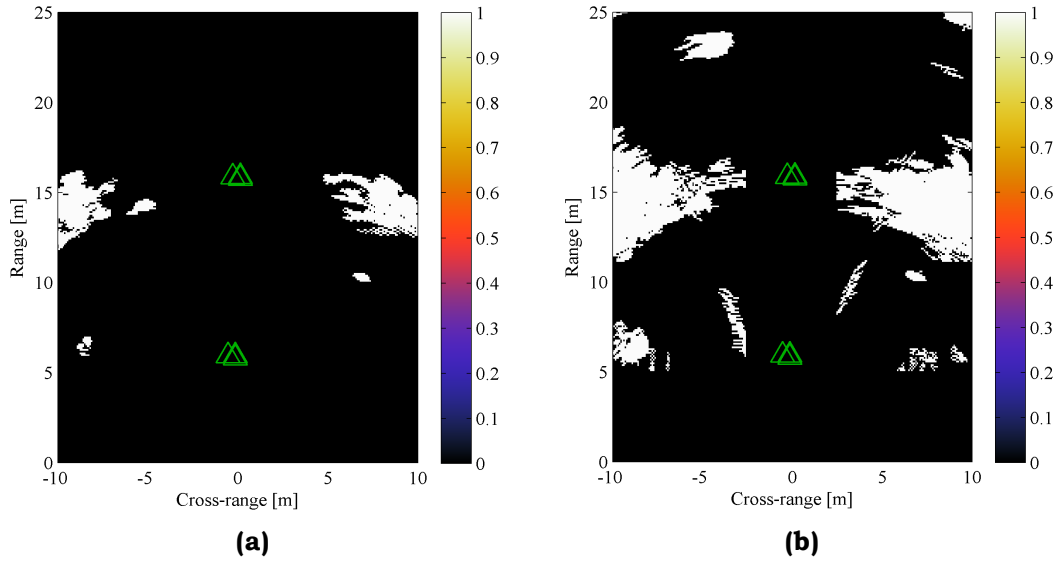

FIG. 6 – Mixed binary mask: **(a)** Fundamental part; **(b)** Extended part. (Δ : True buried target position)

https://doi.org/10.26376/GPR2018011

TABLE II - COMBINATION PATTERN FOR AVERAGE.

Combination index #	**Output images**
0	Original SAR image
1	Iterations 1 and 2 times
2	Iterations 2 and 3 times
3	Iterations 3 and 4 times
4	Iterations 4 and 5 times
5	Iterations 5 and 6 times
6	Iterations 6 and 7 times

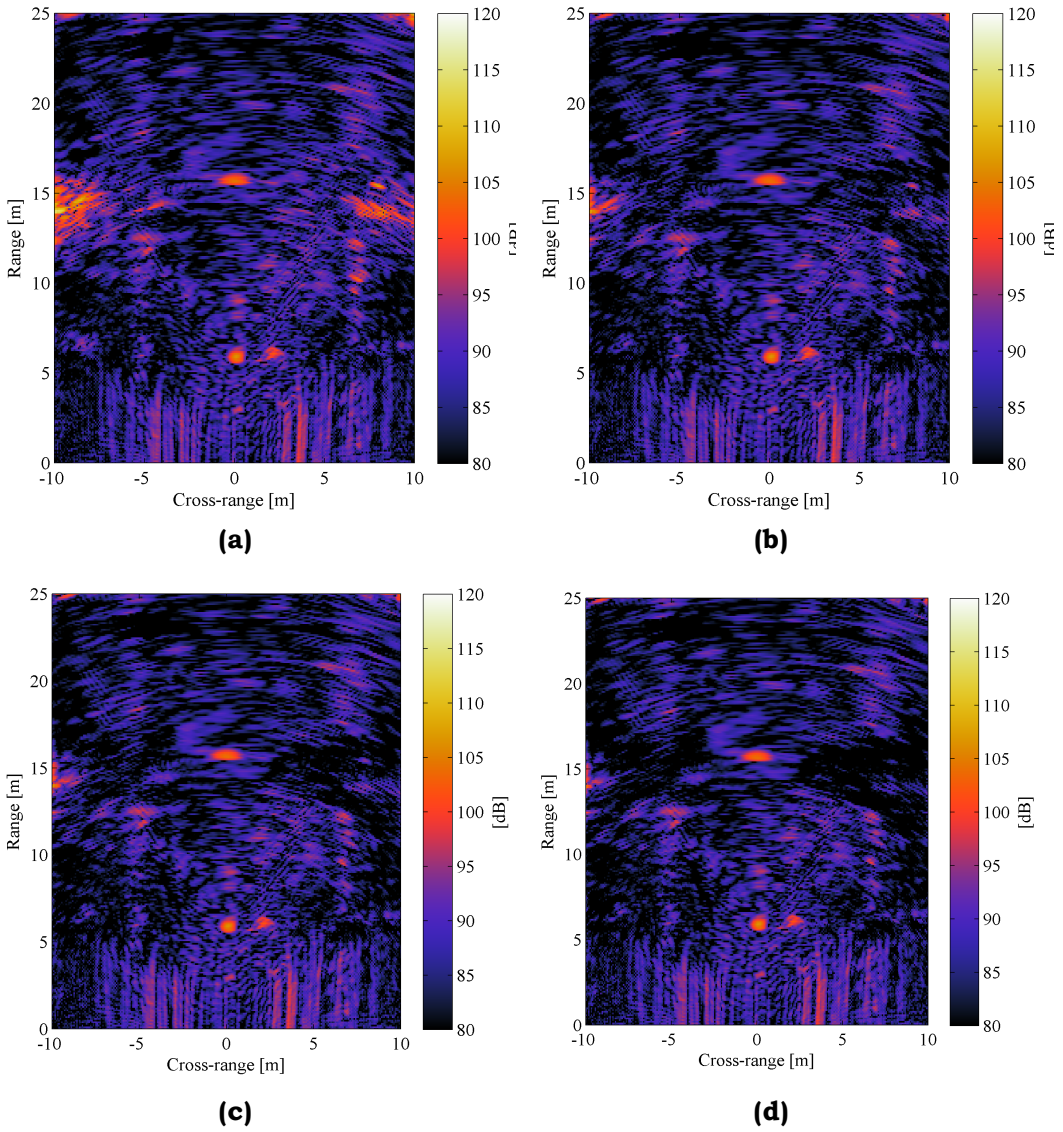

FIG. 7 – Averaging images to reduce clutter: **(a)** #1; **(b)** #3; **(c)** #4; **(d)** #6. Targets are in the same position as in Figure 3(a).

https://doi.org/10.26376/GPR2018011

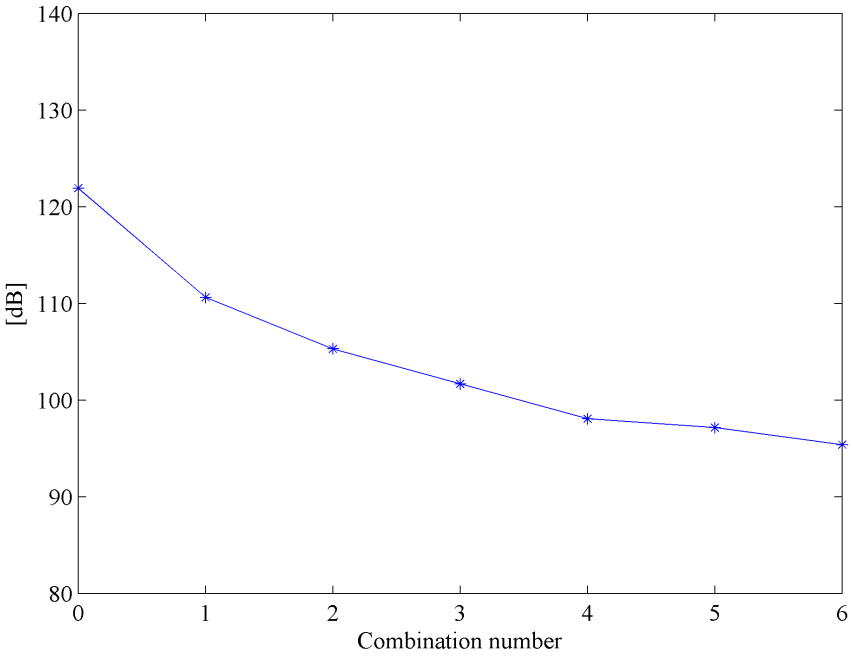

(a)

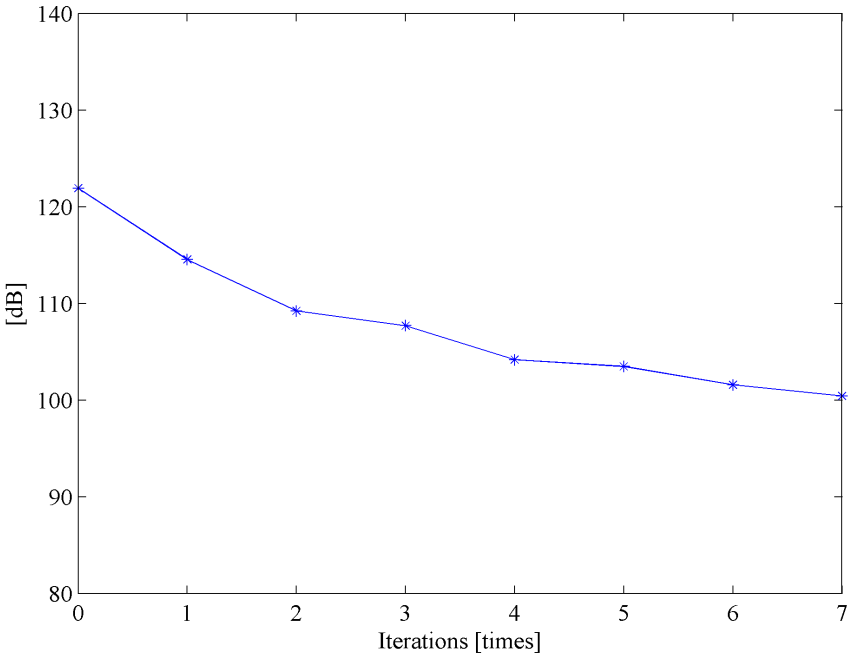

(b)

FIG. 8 – Clutter signal as a function of iteration number and in combination: **(a)** Without averaging; **(b)** With averaging, as indicated by index number.

https://doi.org/10.26376/GPR2018011

4. Evaluation

The proposed method for FLGPR system is validated on two arid test lanes, with metal targets buried at different depths.

The ROC curve quantifies detection performance, presenting the relationship between the probability detection (P_d) and the false alarm rate (FAR). FAR is calculated as the number of false alarms per the total sensing area, and the total sensing area is the accumulated detection area for all measured frames. In this paper, the detection area is set with cross-range span -7 ~ 7 m and down track span 5 ~10 m. The halo area for evaluation of the detected target is a circle centred at the ground truth target, with a diameter of 1 m. A signal is positively declared when it is over the threshold and located within the halo.

The resulting ROC curves in the two lanes are presented in Figure 9. They show the results for the original SAR imaging and the model-based clutter suppression processed SAR image. Based on these figures, the false alarm rate is significantly improved by using the proposed model-based clutter suppression method.

5. Conclusion

An advanced model-based clutter suppression method, which suppresses clutter signals in FLGPR SAR imaging, was presented. The method applies a mixed binary mask created from L-band VV, VH pol image, and X-band SAR images. The effect of the clutter suppression method has been validated with the measurement data. The result of the test lane shows that the method significantly reduces the false alarm rate.

Ackwnowledgement

This paper is supported by United States Army, Communications-Electronics Research, Development and Engineering Center, Night Vision and Electronic Sensors Directorate (W909MY12C0028).

https://doi.org/10.26376/GPR2018011

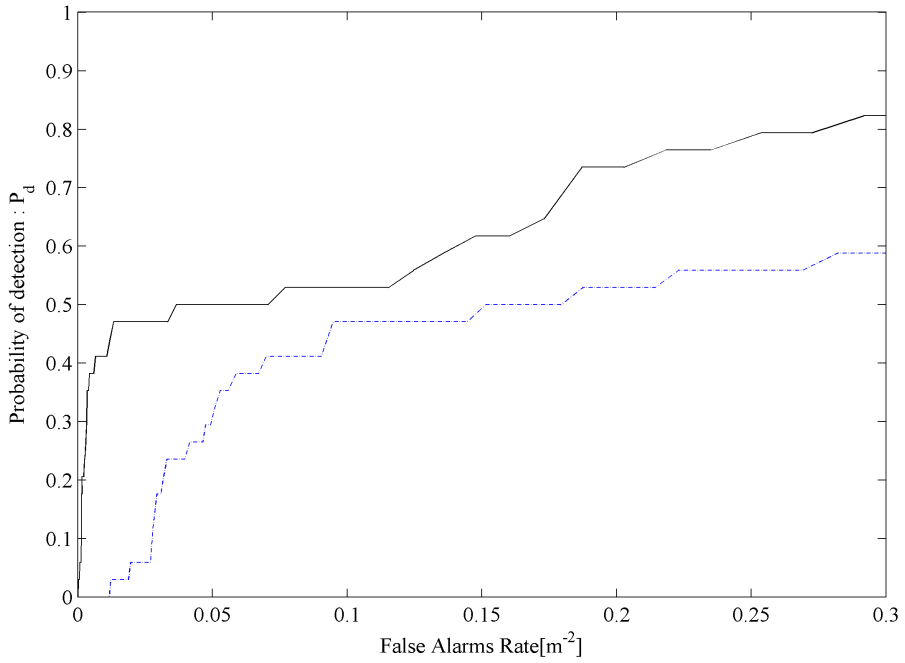

(a)

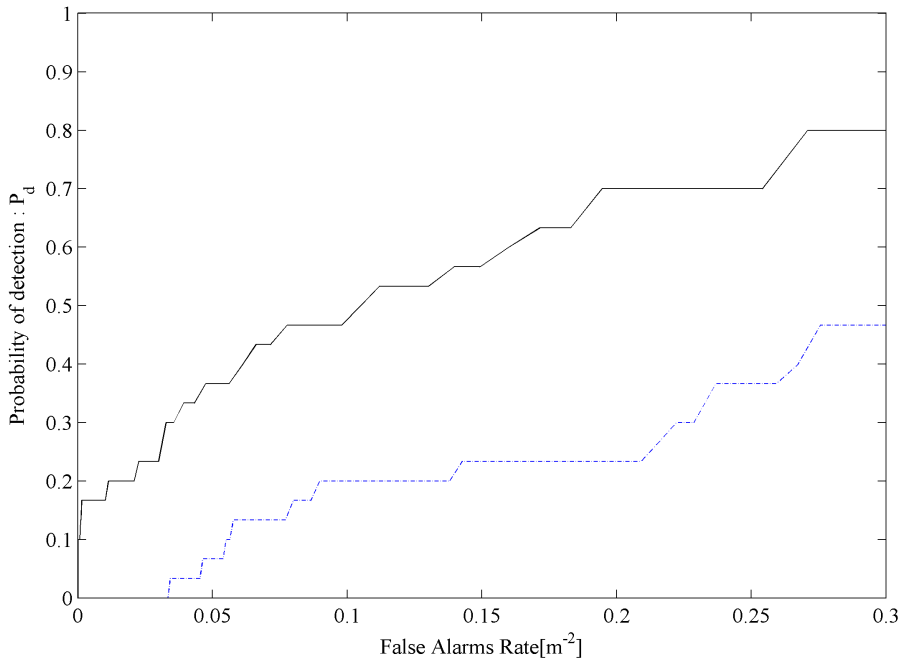

(b)

Fig. 9 – ROC results: **(a)** Lane A; **(b)** Lane B. (--------, With processing; ———, Without processing)

https://doi.org/10.26376/GPR2018011

REFERENCES

[1] D. J. Daniels, "A review of GPR for landmine detection," Sensing and Imaging: An international journal, vol. 7, no. 3, pp. 90–123, September 2006, doi: 10.1007/s11220-006-0024-5.

[2] N. Playle, D. M. Port, R. Rutherford, I. A. Burch, and R. Almond, "Infrared polarization sensor for forward-looking mine detection," 2002 AeroSense conference of the International Society for Optics and Photonics, Orlando, FL, US – Proceedings of the SPIE, vol. 4742: Detection and Remediation Technologies for Mines and Minelike Targets VII, August 2002, pp. 11–18, doi: 10.1117/12.479086.

[3] K. P. Gurton and M. Felton, "Remote detection of buried land-mines and ieds using lwir polarimetric imaging," Optics Express, vol. 20, no. 20, pp. 22344–22359, September 2012, doi: 10.1364/OE.20.022344.

[4] R. D. Costley, J. M. Sabatier, and N. Xiang, "Forward-looking acoustic mine detection system," 2001 Aerospace/Defense Sensing, Simulation, and Controls conference of the International Society for Optics and Photonics, Orlando, FL, US – Proceedings of the SPIE, vol. 4394: Detection and Remediation Technologies for Mines and Minelike Targets VI, October 2001, pp. 617–626, doi: 10.1117/ 12.445514.

[5] J. Moros, F. J. Fortes, J. M. Vadillo, and J. J. Laserna, "Libs detection of explosives in traces," Chapter 13 in Laser-Induced Breakdown Spectroscopy, Springer Series in Optical Sciences, vol. 182, pp. 349–376, 2014, ISBN 9783642450846.

[6] G. Liu, Y. Wang, J. Li, and M. R. Bradley, "SAR imaging for a forward-looking GPR system," 2003 Aerospace/Defense Sensing, Simulation, and Controls conference of the International Society for Optics and Photonics, Orlando, FL, US – Proceedings of the SPIE, vol. 5089: Detection and Remediation Technologies for Mines and Minelike Targets VIII, September 2003, pp. 322–333, doi: 10.1117/12.485687.

[7] T. Ton, D. Wong, and M. Soumekh, "Alaric forward-looking ground penetrating radar system with standoff capability," Proceedings of the 2010 IEEE International Conference on Wireless Information Technology and Systems, 28 August – 3 September 2010, Honolulu, HI, US, pp. 1–4, doi: 10.1109/ ICWITS.2010.5611911.

[8] T. Wang, J. M. Keller, P. D. Gader, and O. Sjahputera, "Frequency subband processing and feature analysis of forward-looking ground-penetrating radar signals for land-mine detection," IEEE Transactions on Geoscience and Remote Sensing, vol. 45, no. 3, pp. 718–729, February 2007, doi: 10.1109/TGRS.2006.888142.

https://doi.org/10.26376/GPR2018011

[9] T. C. Havens, K. Ho, J. Farrell, J. M. Keller, M. Popescu, T. T. Ton, D. C. Wong, and M. Soumekh, "Locally adaptive detection algorithm for forward-looking ground-penetrating radar," 2010 Defense, Security, and Sensing conference of the International Society for Optics and Photonics, Orlando, FL, US – Proceedings of the SPIE, vol. 7664: Detection and Sensing of Mines, Explosive Objects, and Obscured Targets XV, April 2010, Article ID 76642E, 9 pp., doi: 10.1117/12.851512.

[10] T. C. Havens, K. Stone, D. T. Anderson, J. M. Keller, K. Ho, T. T. Ton, D. C. Wong, and M. Soumekh, "Multiple kernel learning for explosive hazard detection in forward-looking ground-penetrating radar," 2012 Defense, Security, and Sensing conference of the International Society for Optics and Photonics, Baltimore, MD, US – Proceedings of the SPIE, vol. 8357: Detection and Sensing of Mines, Explosive Objects, and Obscured Targets XVII, May 2012, Article ID 83571D, 15 pp, doi: 10.1117/12.920482.

[11] D. Anderson, J. M. Keller, and O. Sjahputera, "Algorithm fusion in forward-looking long-wave infrared imagery for buried explosive hazard detection," 2011 Defense, Security and Sensing symposium of the International Society for Optics and Photonics, Orlando, FL, US – Proceedings of the SPIE, vol. 8017: Detection and Sensing of Mines, Explosive Objects, and Obscured Targets XVI, May 2011, Article ID 801722, doi: 10.1117/12.884600.

[12] K. Stone, J. Keller, K. Ho, M. Busch, and P. Gader, "On the registration of FLGPR and IR data for a forward-looking landmine detection system and its use in eliminating FLGPR false alarms," 2008 Defense, Security and Sensing symposium of the International Society for Optics and Photonics, Orlando, FL, US – Proceedings of the SPIE, vol. 6953: Detection and Sensing of Mines, Explosive Objects, and Obscured Targets XIII, April 2008, Article ID 695314, 12 pp. doi: 10.1117/12.782238.

[13] T. C. Havens, C. J. Spain, K. Ho, J. M. Keller, T. T. Ton, D. C. Wong, and M. Soumekh, "Improved detection and false alarm rejection using FLGPR and color imagery in a forward-looking system," in 2010 Defense, Security and Sensing symposium of the International Society for Optics and Photonics, Orlando, FL, US – Proceedings of the SPIE, vol. 7664: Detection and Sensing of Mines, Explosive Objects, and Obscured Targets XV, April 2010, Article ID 76641U, 12 pp., doi: 10.1117/12.852274.

[14] B. Gonzalez-Valdes, Y. Alvarez, J. A. Martinez-Lorenzo, F. Las-Heras, and C. M. Rappaport, "On the combination of SAR and model based techniques for high-resolution real-time two-dimensional reconstruction," IEEE Transactions on Antennas and Propagation, vol. 62, no. 10, pp. 5180–5189, October 2014, doi: 10.1109/TAP.2014.2346203.

https://doi.org/10.26376/GPR2018011

[15] Y. Fuse, B. Gonzalez-Valdes, J. A. Martinez-Lorenzo, and C. M. Rappaport, “Advanced SAR imaging methods for forward-looking ground penetrating radar,” Proceedings of the 10th European Conference on Antennas and Propagation (EuCAP 2016), Davos, Switzerland, 10–15 April 2016, pp. 1–4, doi: 10.1109/EuCAP.2016.7481192.

https://doi.org/10.26376/GPR2018011

The scientific paper that you have downloaded is included in Issue 2, Volume 1 (July 2018) of the journal *Ground Penetrating Radar* (ISSN 2533-3100; journal homepage: www.gpradar.eu/journal).
All *Ground Penetrating Radar* papers are processed and published in true open access, free to both Authors and Readers, thanks to the generous support of TU1208 GPR Association and to the voluntary efforts of the journal Editorial Board. The publication of Issue 2, Volume 1 is also supported by Adapis Georadar Teknik Ab (georadar.eu) and by IDS Georadar s.r.l. (idsgeoradar.com).
The present information sheet is obviously not part of the scientific paper.